Intense Equatorial Electrojet and Counter Electrojet caused by the 15 January 2022 Tonga Volcanic Eruption: Space and Ground-based Observations

Guan Le[1], Guiping Liu[1,2,3], Endawoke Yizengaw[4], Christoph R. Englert[5]

1. ITM Physics Laboratory, Heliophysics Division, NASA Goddard Space Flight Center, Greenbelt, MD
2. The Catholic University of America, 620 Michigan Ave., N. E., Washington, DC
3. Space Sciences Laboratory, University of California, Berkeley, CA
4. Space Science Application Laboratory, The Aerospace Corporation, 2310 E. El Segundo Blvd., El Segundo, CA
5. Space Science Division, U.S. Naval Research Laboratory, Washington, DC

Submitted to Geophysical Research Letters on 4/5/2022

Revision 5/5/2022

Paper Number: 2022GL099002

Key Points (maximum 140 characters per line):

- Space and ground-based observations reveal dramatic equatorial electrojet variations caused by the Tonga volcanic eruption
- Strong eastward turning of atmospheric zonal winds in the E-region is responsible for the directional reversal of the equatorial electrojet
- The observed complex spatiotemporal variations can be explained by a large-scale disturbance propagating eastward from the eruption site

Abstract

We present space and ground-based multi-instrument observations demonstrating the impact of the 2022 Tonga volcanic eruption on dayside equatorial electrodynamics. A strong counter electrojet (CEJ) was observed by Swarm and ground-based magnetometers on 15 January after the Tonga eruption and during the recovery phase of a moderate geomagnetic storm. Swarm also observed an enhanced equatorial electrojet (EEJ) preceding the CEJ in the previous orbit. The observed EEJ and CEJ exhibited complex spatiotemporal variations. We combine them with the Ionospheric Connection Explorer (ICON) neutral wind measurements to disentangle the potential mechanisms. Our analysis indicates that the geomagnetic storm had minimal impact; instead, a large-scale atmospheric disturbance propagating eastward from the Tonga eruption site was the most likely driver for the observed intensification and directional reversal of the equatorial electrojet. The CEJ was associated with strong eastward zonal winds in the E-region ionosphere, as a direct response to the lower atmosphere forcing.

Key Words

Tonga Volcanic Eruption, Equatorial Electrojet, Counter Electrojet, Equatorial Electrodynamics, Equatorial Electric Field, Atmospheric Neutral Winds

Plain Language Summary

The Earth's E-region ionosphere (~100-150 km altitude) consists of both ionized and neutral gasses, and the two components are coupled through ion-neutral collisions. The state of this region is closely influenced by neutral atmospheric activities from the lower atmosphere and the variability of the solar drivers. On 15 January 2022, the Tonga volcano had a massive eruption and injected an enormous amount of mass and energy into the atmosphere causing disturbances in the E-region ionosphere or even higher. There was also a moderate geomagnetic storm that started one day before the eruption and ended days after. These conditions offer a unique opportunity to understand the different roles they play in controlling the ionosphere. Coordinated observations including the atmosphere, ionosphere and magnetosphere were made from both space and on the ground during this event. We analyzed the magnetic field and neutral wind data and found that a large-scale atmospheric disturbance generated by the volcano eruption was responsible for the observed directional reversal of the dayside equatorial electric field and electric current.

1. Introduction

The equatorial electrojet (EEJ) is an intense band of ionospheric electric current flowing eastward along the dayside magnetic equator. The peak of the EEJ occurs near noon in the E-region ionosphere (~ 110 km altitude), where a local conductivity maximum is produced by the balance between the photoionization from solar radiation and chemical losses (e.g., Heelis and Maute, 2020). The EEJ results from distinctive E-region electrodynamic processes involving both atmospheric neutrals and collisional plasma in a geometry with a horizontally northward geomagnetic field at the magnetic equator. During solar and geomagnetically quiet times, an eastward zonal electric field is generated in the dayside by plasma-neutral collisional interactions as atmospheric tidal winds move ionospheric plasma across magnetic field lines (known as E-region wind dynamo) (Richmond, 1973; Heelis, 2004). The current density of the EEJ can be readily measured in the magnetic field data both on the ground (Anderson et al., 2004; Yizengaw et al., 2014) or by low-Earth orbit spacecraft (Lühr et al., 2004; Alken et al., 2015).

Observations show that the EEJ exhibits much variability with longitude as well as on multiple temporal scales (e.g., Lühr et al., 2004; Yizengaw and Groves, 2018). Sometimes the EEJ can even experience directional reversals, known as counter electrojets (CEJ) (e.g., Forbes, 1981). The main causes of the EEJ variations are attributed to the electric field perturbations, which can be driven either through enhanced solar wind-magnetosphere-ionosphere coupling (e.g., Yizengaw et al., 2016), or by neutral wind perturbations from lower atmosphere forcing (e.g., Yamazaki et al., 2014). Variations of the EEJ have been used as an indirect measure of the E-region electric field perturbations as well as F-region $\boldsymbol{E} \times \boldsymbol{B}$ drift.

The main driving mechanism for the EEJ variability is the modulation of the E-region wind dynamo. During the normal eastward EEJ the zonal winds across E-region altitudes are mostly in the westward direction whereas the winds reverse to be eastward at ~110 km altitude during the westward CEJ (Yamazaki et al., 2021). Vertically propagating atmospheric tidal waves can produce wind variations on the order of tens of m/s (e.g., Hagan and Forbes, 2002). These tidal winds directly produce the longitudinal and daily variations of the EEJ (e.g., Forbes, 1981; Lühr et al., 2021). Large amplitude planetary waves such as 3-day waves could modulate the wind dynamo and thereby drive the multi-day periodic variations (e.g., Forbes et al., 2018; Liu et al., 2021). In addition, smaller-scale waves, such as gravity waves triggered by geological phenomena, such as earthquakes and tsunamis, can also induce short-period fluctuations in the EEJ and the electric fields (e.g., Aveiro et al., 2009; Hysell et al., 1997).

Prompt penetration electric field (PPEF) during geomagnetically active times is an additional source of variations in the low-latitude E-region (e.g., Fejer et al., 1979; Wolf et al., 2007). During geomagnetic storms, extreme changes of the EEJ, both enhancement and directional reversals (CEJ), have been observed nearly instantaneously following the interplanetary magnetic field (IMF) changes and rapid variations of the Region-1 field-aligned currents (FACs) that lead to undershielding and overshielding conditions, respectively (Kelley et al., 1979; Kikuchi et al., 2000; Sastri, 2002; Simi et al., 2012; Yizengaw et al., 2016; Astafyeva et al., 2019). The high-latitude ionosphere can also affect the middle- and low-latitudes through disturbance winds during geomagnetic storms, known as disturbance dynamo (Fejer et al., 1983). Unlike the PPEF, disturbance dynamo electric fields have delayed responses to the high latitude heating events (Richmond and Matsushita, 1975; Scherliess and Fejer, 1997; Fuller-Rowell et al., 2002).

On 15 January 2022, the Swarm spacecraft observed a much-enhanced EEJ and then a strong CEJ in two consecutive orbits (~ 1.5 hr apart). On the same day, a ground-based magnetometer pair near the magnetic equator, Jicamarca and Tarapoto, observed an intense CEJ first but then the normal EEJ. The EEJ and CEJ observed from space and on the ground exhibited complex spatiotemporal variations. The event occurred during a period when both the magnetospheric forcing and the atmospheric forcing coexisted: a moderate geomagnetic storm and the Tonga volcanic eruption, respectively. In this paper, we present a detailed analysis of the observations from multiple sources, including the IMF and solar wind, ground-based and spacecraft magnetic fields, and atmospheric neutral winds to determine the role of these potential sources on perturbing the equatorial E-region electric field. The goal is to disentangle the mechanisms responsible for the observed intensification and directional reversal of the equatorial electrojet.

2. Dataset Description

Swarm is a three-spacecraft mission in high-inclination (87.5°) low-Earth orbit (Friis-Christensen et al., 2006). Swarm-A&C fly side by side at ~430 km (at the start of 2022) with a longitudinal separation of 1.4° and Swarm-B is slightly higher at ~500 km. With an orbit period of ~90 min, the spacecraft crosses the polar cap every ~45 mins and the EEJ every ~1.5 hrs. Highly accurate data from Swarm's Vector Field Magnetometer (VFM) provide in-situ measurements of FACs in the auroral zone (Lühr et al., 2015; 2016). The magnetic field strength from the Absolute Scalar Magnetometer (ASM) measurements have been used to obtain the amplitude and direction of the EEJ (Alken et al., 2015; Lühr et al., 2021).

The EEJ signals are also obtained from a pair of ground magnetometer stations located near the magnetic equator on the same meridian, one at the magnetic equator (within 3.5°) and the other one just off the EEJ region (6° to 9° degree from the magnetic equator) (Anderson et al., 2004; Yizengaw et al., 2014). The EEJ currents are determined from δH, the difference of the magnetic field H-components between the two magnetometers (Anderson et al., 2004; Yizengaw et al., 2014). The pair of the ground stations we used in this study are located at Jicamarca (JICA, 11.95^{o}N/76.87^{o}W GEO, MLat=0.6^o) and Tarapoto (TARA, 6.59^{o}N/76.36^{o}W GEO, Mlat= 6^o) in Peru.

The neutral wind measurements are provided by the Michelson Interferometer for Global High-Resolution Thermospheric Imaging (MIGHTI) (Englert et al., 2017) on the 27^o low-inclination Ionospheric Connection Explorer (ICON) mission (Immel et al., 2018). Using Doppler shifts, atmospheric wind velocities are derived from the O(^{1}S) (557.7 nm, green line) and O(^{1}D) (630.0 nm, red line) airglow emissions at ~3 and ~10 km altitude bins, respectively across the range from ~90 to 300 km. The MIGHTI winds have been validated with the ground-based measurements showing a correlation of ~0.8 (Harding et al., 2021; Makela et al., 2021). The MIGHTI winds cover low-to-mid latitudes from ~13^{o}S to 42^{o}N, and for each day the data are available from ~15 orbits with two local times sampled at the same latitude per orbit.

3. Observations

On 14 January 2022, a moderate geomagnetic storm (minimum Dst ~ -91 nT) was triggered by the arrival of a coronal hole high-speed solar wind stream. Figure 1 shows the 5-min resolution OMNI data with IMF/solar wind conditions and SYM-H index for 13-16 January. The start times for the storm’s main and recovery phases are indicated by the two black arrows on the top, respectively. The storm's main phase was caused by a gradual southward turning of the IMF Bz which lasted for ~ 7 hours (~16-23 UT on 14 January). The recovery phase started when the IMF Bz suddenly turned strongly northward, associated with a minor shock, and then fluctuated between northward and southward directions. It took about 5 days for the magnetosphere to fully recover. On 15 January, coincident with the early recovery phase, a powerful, quasi-continuous eruption of the Hunga Tonga-Hunga Ha'apai Volcano occurred about 65 km north of Tonga's main island, starting at ~0402 UT for about 12 hours, which is indicated as the magenta bar on the top of Figure 1. Atmospheric waves produced by the eruption were observed globally (Yuen et al., 2022; Zhang et al., 2022). These are the background conditions under which the 15 January EEJ and CEJ events were observed.

Figure 2 presents an overview of the observations. Figure 2a displays 5 days of the magnetic field perturbations (13-17 January) from Swarm A. The red traces are the azimuthal component of the perturbations over the polar cap from Swarm A's VFM. The magnetic field perturbations in high latitudes are mainly caused by FACs, and the azimuthal component (δB_FAC, positive for westward deflection) is expected to bear the largest FAC signatures (Le et al., 2016). The black traces in Figure 2a are the perturbations of the field strength during the equatorial crossing over the EEJ region (within 10^{o} latitude from the dayside magnetic equator) from Swarm A's ASM. The eastward EEJ would cause a magnetic field depression ($\delta B<0$) and the westward CEJ a field enhancement ($\delta B>0$).

On 14 January, the magnitude of δB_FAC was enhanced to ~500 nT after the storm onset at ~ 16 UT. But the EEJ did not change markedly compared with the previous EEJ passes, indicating the lack of the penetration electric field. This is most likely due to the rather gradual southward turning of the IMF, under which conditions the shielding of the convection electric field in middle and low latitudes was still effective. The intensity of the EEJ remained relatively stable until around ~ 14 UT on 15 January, when a much enhanced EEJ was observed by Swarm, denoted by 1 in Figure 2a and the blue arrow on top of Figure 1. A very strong CEJ was observed subsequently by Swarm in the next dayside equatorial pass at around 15.5 UT, denoted by 2 in Figure 2a and the red arrow on top of Figure 1. Figure 2c shows an expanded view of the Swarm observation for 1200-1725 UT on 15 January, containing the observations from both Swarm A and B. Similar to Swarm A, Swarm B also observed the much enhanced EEJ and then the strong CEJ, but its δB magnitudes were smaller because of its higher altitude. The geographic locations of Swarm A and B for the dayside equatorial passes near local noon are shown in Figure 2d as the line segments in black and gray, respectively. The CEJ region at ~ 15.5 UT was observed to the west of the EEJ region observed at ~ 14 UT although Swarm's local time remained to be the same, near local noon.

Figure 2b shows the ground-based observations near the magnetic equator for 13-17 January. The solid black traces are for δH, the differences between the H-components recorded at the geomagnetic equator (JICA) and off the equator (TARA). The red traces are the estimated $\boldsymbol{E}\times\boldsymbol{B}$ drift in the F-region based on δH using the technique described in Anderson et al. (2004). Note that the data from JICA and TARA were not recorded on 16 January, and we used the data from Huancayo (HUA, 12.05°S/75.33°W GEO, Mlat=-0.63°) and San Juan (SJG, 18.11°N/66.15°W GEO, Mlat=28.79°) to obtain δH (dotted line). Since the location of SJG is not ideal for EEJ estimation, these δH data are used only for obtaining general information about the EEJ behavior, rather than a quantitative comparison with the other days. The start times for the Tonga eruption and the storm main and recovery phases are indicated by the arrows in the 14 January panel. We note that the ground stations did not measure significantly different EEJ strengths between 13 and 14 January. In addition, no significant changes, instantaneous or delayed, were observed at the storm onset and recovery on 14 January. These observations indicate that the storm's impact on the equatorial electric field was minimal in this case, consistent with the Swarm observations.

On 15 January, JICA immediately observed a CEJ period with the strong magnetic field depression (δH<0) at ~12 UT (~ 7 local time), which is about the same time as it began to detect the normal EEJ region in previous days. This means the CEJ was probably already present before ~12 UT. After ~ 4 hr, JICA transitioned into an EEJ region (δH>0) at ~15.5 UT (~10.5 local time). The peak magnitude of δH in the EEJ region was only slightly larger than the previous two days, so it appeared to be a nominal EEJ. During the following two days (16 and 17 January), only normal EEJ was observed. In Figure 2d, the geographic location of JICA is marked as a red triangle. The CEJ was also observed on the ground to the west of the Swarm CEJ locations.

We now focus on how neutral wind perturbations caused the electric field perturbations. On 15 January, the ICON spacecraft observed neutral winds for the same regions and times as Swarm and JICA. Figure 2d marks the locations (blue dots) and the UT times of the daytime low-latitude zonal winds (from green-line emission, ~6-9 LT, < 25^o latitude) measured by MIGHTI on ICON. Due to the low-inclination, MIGHTI samples a relatively wide range of longitudes during each orbit pass. The zonal winds observed along 7 orbits (each ~1.5 hr apart and during <10 minutes time interval) are presented in Figure 3. The brown curve passing through JICA (red triangle) is a part of the circle centered at the Tonga eruption site, showing locations of equal distance from the eruption site. At ~14 UT, the ICON observations were located across the brown curve, MIGHTI and JICA would thus concurrently detect the wind perturbations propagating from the eruption site. The observations for a few hours before and after 14 UT are also shown.

Figures 3a and 3b display the zonal wind sequences and averaged profiles, respectively, observed at the given times and locations. The wind components have been transformed into the local magnetic coordinates assuming zero vertical winds. At ~13.9 UT, eastward winds dominated across the E-region altitudes from ~95-120 km, and the largest winds reached ~200 m/s with the averaged peak values of ~150 m/s (meridional winds were southward at ~ 30 m/s at this time). Strong eastward winds are thus observed in the E-region in coincident with the strong CEJ at JICA. In the observations before this, at ~12.3 UT, both eastward and westward winds were observed around 67.5°W longitudes. In particular, below ~110 km, the winds changed from mostly eastward to mostly westward in the wind profile sequence (the 4th panel in Figure 3a) as the MIGHTI observation locations moved from 80°W to 65°W longitudinally (blue dots in Figure 2d). This indicates the transition region from the CEJ (eastward winds) to EEJ (westward winds). The winds were weaker in other times before ~12.3 UT and after ~13.9 UT. The winds were <100 m/s and tended to gradually turn westward at ~15.5 and 17.1 UT. The winds were also almost all westward throughout the altitude region at ~7.5 UT. From ~9.1 to ~10.7 UT, the winds remained westward at most altitudes and were barely eastward only around 105 km.

Figure 3c presents the sequence of zonal wind observations at ~103 km altitude versus longitude. Compared to the day before (in black), the dayside zonal winds on 15 January (blue) exhibited a large variation having strong eastward winds over ~60° - 120° W longitudes. This is again consistent with the directional turning from the EEJ to CEJ.

4. Discussion

The observations presented in the previous section showed complex spatiotemporal variations of the CEJ and EEJ, which can be explained by a large-scale disturbance propagating eastward from the Tonga eruption site. As illustrated in Figure 4a, the light green and blue areas represent the leading and trailing fronts of the disturbance, respectively. The leading front is associated with a westward neutral wind perturbation, which reinforces the background westward wind in the dayside and causes an increase in the eastward electric field. This front is expected to result in an enhanced EEJ region that has been observed by Swarm. The trailing front is associated with a strong eastward wind perturbation, which is opposite to the background wind and thus reverses the electric field causing the directional reversal of the EEJ (i.e., CEJ) and downward vertical drift inferred by JICA. This explanation is further illustrated in Figure 4b and the timelines of the observed features are summarized as follows.

- **At ~12.5 UT** (Figure 4b – top panel): The wind disturbance fronts had moved to cross the day-night terminator and had reached the ICON measurement locations, but it had not yet reached the Swarm location, so that a nominal EEJ was observed by Swarm (see Figure 2c). Furthermore, JICA just emerged from the nightside and entered directly into the trailing front to start detecting the CEJ, but completely missed the leading front for the enhanced EEJ (Figure 2b). Because the ICON measurements were near the center of the disturbance moving from trailing to leading fronts, eastward and then westward zonal winds were observed (Figure 3a). Given (1) that JICA observed the CEJ approximately 8 hours after the volcanic eruption and (2) the great circle distance from JICA to Tonga is ~10,000 km, the speed of the propagating disturbance was estimated to be at least ~350 m/s. Because the CEJ may have arrived before JICA turned into sunlit conditions, the disturbance could have been propagating faster.
- **At ~14 UT** (Figure 4b, 2^{nd} panel from the top): The disturbance continued its eastward propagation. Swarm's next equatorial crossing cut through the leading front so that a much enhanced EEJ was observed (see Figure 2c). Based on Swarm A's timing (~10 hr) and the great circle distance from the eruption site (~14,000 km), the speed of the leading

front was estimated to be ~400 m/s. JICA remained within the trailing front and thus still observed the CEJ (Figure 2b). At this time, the wind observations were relatively further away from the magnetic equator (covering ~15-25^{o} geographic latitudes). However, all wind profiles in the observation sequence showed eastward winds across ~95-110 km altitudes (5th panel in Figure 3a). This suggests that the ICON measurements were within the trailing front (and at the same distance to Tonga as JICA) and strong eastward zonal winds were observed (Figure 3), which is consistent with the CEJ observation at JICA. This demonstrated the CEJ was caused by the Tonga eruption associated wind perturbation that changed the dayside zonal wind to eastward in the E-region.

- **At ~15.5 UT** (Figure 4b – 3rd panel from the top): Swarm crossed the equatorial region inside the trailing front and was able to detect the strong CEJ (see Figure 2c). However, the front almost moved away from JICA as the JICA meridian was exiting from the CEJ region into the normal EEJ region (Figure 2b). Based on these timings, the CEJ observations by JICA lasted for ~ 3 hr and thus, the scale size of the disturbance is estimated to be on the order of ~5,000 km. On the other hand, the location of the ICON measurements was far to the west of the disturbance, near the terminator, and weaker winds were observed.
- **At ~17 UT** (Figure 4b – bottom panel): The disturbance had propagated further east. Both Swarm and JICA were completely outside the disturbance region to the west and observed regular EEJ current (see Figures 2b and 2c). ICON was even further away from the disturbance and also near the terminator and thus observed weaker winds.

The disturbance responsible for the observed EEJ and CEJ signatures is most likely related to atmospheric gravity wave activities that were produced by the Tonga volcanic eruption and detected globally within the first few hours of the eruption (Yuen et al., 2022). This volcanic eruption generated a broad spectrum of atmospheric waves, such as gravity waves, that propagated into the upper atmosphere and even affected the F-region ionosphere (Zhang et al., 2022; Themens et al., 2022). By combining space and ground-based observations, our analysis shows that this disturbance propagated outward (mainly eastward at our observation locations) from the volcano eruption site with a propagation speed in the order of ~350-400 m/s. We also found that the disturbance has a spatial scale size of ~5,000 km in which the zonal wind perturbation reached up to ~200 m/s. These fall within the features of gravity waves that have been identified before for driving F-region ionospheric irregularities (e.g. Yizengaw and Groves, 2020), as well as those reported for the Tonga volcanic eruption (Yuen et al., 2022; Zhang et al., 2022; Themens et al., 2022). Such a large wind disturbance should be able to significantly modify the E-region dynamo and cause the dramatic variations on the equatorial electric field and current, as the observations we present revealed.

5. Summary and Conclusions

We present multi-instrument observations demonstrating the impact of the 15 January 2022 Tonga volcanic eruption on dayside equatorial electrodynamics. The Tonga eruption coincided with the early recovery phase of the 14-17 January 2022 geomagnetic storm. A strong CEJ was observed by both the Swarm satellites and JICA ground-based magnetometers on 15 January after the Tonga eruption and during the storm recovery phase. The CEJ observed by Swarm was preceded by a much-enhanced EEJ in the previous orbit about 1.5 hours earlier. But JICA observed a normal EEJ after leaving the CEJ region. The EEJ and CEJ, observed both in space and on the ground, exhibited complex spatiotemporal variations. We linked the magnetic field observations in coincidence with atmospheric neutral wind observations from ICON to disentangle the potential mechanisms. Our analysis indicates that the moderate geomagnetic storm on 14-17 January had minimal impact on the equatorial electric field. Instead, large-scale atmospheric disturbances propagating outward/eastward from the Tonga eruption site were the most likely driver for the observed intensification and directional reversal of the equatorial electrojet. We propose that the reversal of the equatorial electrojet is attributed to the strong eastward turning of atmospheric zonal winds in the E-region. While the leading wave front appeared to enhance the westward zonal winds responsible for the observed EEJ intensification, the trailing wave front caused strong eastward zonal winds resulting in the strong CEJ in the E-region ionosphere.

Data Availability Statement

The OMNI data are available at https://omniweb.gsfc.nasa.gov. Swarm data are accessible at https://earth.esa.int/eogateway/missions/swarm/data. The ICON data are available at https://icon.ssl.berkeley.edu/Data. The JICA and TARA magnetometer data are available at http://doi.org/10.5281/zenodo.6412518. The HUA and SJG magnetometer data are available at https://intermagnet.github.io.

Acknowledgements

We thank R. Pfaff, H. Lühr and T. Immel for helpful discussions. G. Liu was partially supported by NASA grants 80NSSC20K1323 and 80NSSC18K0649. E. Yizengaw's work was partially supported by AFOSR (FA9550-20-1-0119) and NSF (AGS-1848730) grants. ICON was supported by NASA contracts NNG12FA45C and NNG12FA42I.

References

Alken, P., S. Maus, A. Chulliat, P. Vigneron, O. Sirol, and G. Hulot (2015), Swarm equatorial electric field chain: First results, Geophys. Res. Lett., 42, 673–680. https://doi.org/10.1002/2014GL062658

Anderson, D., A. Anghel, J. Chau, and O. Veliz (2004), Daytime vertical E × B drift velocities inferred from ground-based magnetometer observations at low latitudes, SpaceWeather, 2, S11001. https://doi.org/10.1029/2004SW000095

Astafyeva, E., I. Zakharenkova, and P. Alken (2016), Prompt penetration electric fields and the extreme topside ionospheric response to the June 22-23, 2015 geomagnetic storm as seen by the Swarm constellation, Earth, Planets and Space, 68:152. https://doi.org/10.1186/s40623-016-0526-x

Aveiro, H.C., C.M. Denardini, & Abdu, M.A. (2009). Climatology of gravity waves-induced electric fields in the equatorial E- region. *Journal of Geophysical Research*, *114*, A11308. http://doi.org/10.1029/2009JA014177

Englert, C.R., Harlander, J.M., Brown, C.M., Marr, K.D., Miller, I.J., Stump, J.E., Hancock, J., Peterson, J.Q., Kumler, J., Morrow, W.H., Mooney, T.A., Ellis, S., Mende, S.B., Harris, S.E., Stevens, M.E., Makela, J.J., Harding, B.J., & Immel, T.J. (2017). Michelson Interferometer for Global High-resolution Thermospheric Imaging (MIGHTI): instrument design and calibration. *Space Science Reviews*, *212*(1-2), 553-584. https://doi.org/10.1007/s11214-017-0358-4

Fejer, B. G., C. A. Gonzales, D. T. Farley, M. C. Kelley, and R. F. Woodman (1979), Equatorial electric fields during magnetically disturbed conditions: The effect of the interplanetary magnetic field, J. Geophys. Res.,84, 5797–5802. http://doi.org/10.1029/JA084iA10p05797

Fejer, B. G., M. F. Larsen, and D. T. Farley (1983), Equatorial disturbance dynamo electric fields, Geophys. Res. Lett., 10, 537-540. https://doi.org/10.1029/GL010i007p00537

Forbes, J.M. (1981). The equatorial electrojet. *Review of Geophysics*, *19*(3), 469-504. https://doi.org/10.1029/rg019i003p00469

Forbes, J.M., Maute, A., Zhang, X., & Hagan, M.E. (2018). Oscillation of the ionosphere at planetary-wave periods. *Journal of Geophysical Research*, *123*, https://doi.org/10.1029/2018JA025720

Friis-Christensen, E., H. Lühr, and G. Hulot (2006), Swarm: A constellation to study the Earth's magnetic field, Earth Planets Space, 58, 351–358. https://doi.org/10.1186/BF03351933

Hagan, M.E., and Forbes, J.M. (2002). Migrating and nonmigrating diurnal tides in the middle and upper atmosphere excited by tropospheric latent heat release. *Journal of Geophysical Research*, *107*(D24), 4754. https://doi.org/10.1029/2001JD001236

Harding, B.J., Chau, J.L., He, M., Englert, C.R., Harlander, J.M., Marr, K.D., et al. (2021). Validation of ICON-MIGHTI thermospheric wind observations: 2. Green-line comparisons to specular meteor radars. *Journal of Geophysical Research*, *126*, 2020JA028947. https://doi.org/10.1029/2020JA028947

Heelis, R.A. (2004). Electrodynamics in the low and middle latitude ionosphere: a tutorial. *Journal of Atmospheric and Solar-Terrestrial Physics*, *66*, 825-838. https://doi.org/10.1016/j.jastp.2004.01.034

Heelis, R. A., & Maute, A. (2020). Challenges to understanding the Earth's ionosphere and thermosphere. Journal of Geophysical Research: Space Physics, 125, e2019JA027497. https://doi.org/10.1029/2019JA027497

Hunsucker, R. D (1982), Atmospheric gravity waves generated in the high-latitude ionosphere: A review, Reviews of Geophysics, 20, 293-315. https://doi.org/10.1029/RG020i002p00293

Hysell, D.L., J.L. Chau, & Fesen, C.G. (2002). Effects of large horizontal winds on the equatorial electrojet. *Journal of Geophysical Research*, *107*(A8), SIA 27-1-SIA 27-12. https://doi.org/10.1029/2001JA000217

Hysell, D. L., M. F. Larsen, and R.F. Woodman (1997). JULIA radar studies of electric fields in the equatorial electrojet, Geophys. Res. Lett., 24 (13) (1997), pp. 1687-1690. https://doi.org/10.1029/97GL00373

Immel, T.J., England, S.L., Mende, S.B. et al. (2018). The Ionospheric Connection Explorer mission: mission goals and design. *Space Science Reviews*, *214*. https://doi.org/10.1007/s11214-017-0049-2

Kelley, M. C., B. G. Fejer, and C. A. Gonzales (1979), An explanation for anomalous equatorial ionospheric electric fields associated with a northward turning of the interplanetary magnetic field, Geophys. Res. Lett., 6, 301. http://doi.org/10.1029/GL006i004p00301

Kikuchi, T., H. Luhr, T. Kitamura, O. Saka, and K. Schlegel (1996), Direct penetration of the polar electric fields to the equator during a DP 2 event as detected by the auroral and equatorial magnetometer chains and the EISCAT radar, *J. Geophys. Res*., 101, 17,161–17,173. https://doi.org/10.1029/96JA01299

Kikuchi, T., H. Luhr, K. Schlegel, H. Tachihara, M. Shinohara, and T.L. Kitamura (2000), Penetration of auroral electric fields to the equator during a substorm, *J. Geophys. Res*., 105, 23,251–23,252. https://doi.org/10.1029/2000JA900016

Le, G., et al. (2016),Magnetopause erosion during the 17 March 2015 magnetic storm: Combined field-aligned currents, auroral oval, and magnetopause observations, Geophys. Res. Lett., 43. https://doi.org/10.1002/2016GL068257

Liu, G., England, S. L., Lin, C. S., Pedatella, N. M., Klenzing, J. H., Englert, C. R., et al. (2021). Evaluation of atmospheric 3-day waves as a source of day-to-day variation of the ionospheric longitudinal structure. *Geophysical Research Letters*, *48*, e2021GL094877. https://doi.org/10.1029/2021GL094877

Lühr, H., J. Park, J. W. Gjerloev, J. Rauberg, I. Michaelis, J. M. G. Merayo,and P. Brauer (2015), Field-aligned currents' scale analysis per-formed with the Swarm constel-lation,Geophys. Res. Lett., 42, 1–8. http://doi.org/10.1002/2014GL062453

Lühr, H., T. Huang, S. Wing, G. Kervalishvili, J. Rauberg, and H. Korth (2016), Filamentary field-aligned currents at the polar cap region during northward interplanetary magnetic field derived with the Swarm constellation, Ann. Geophys., 34, 901–915. https://doi.org/10.5194/angeo-34-901-2016

Lühr, H., Zhou, Y.-L., & Alken, P. (2021). Short-term variability of equatorial electrojet modulation by solar tidal and planetary waves, as derived from the Swarm constellation. Journal of Geophysical Research: Space Physics, 126, e2020JA028884. https://doi.org/10.1029/2020JA028884

Makela, J. J., Baughman, M., Navarro, L. A., Harding, B. J., Englert, C. R., Harlander, J. M., et al. (2021). Validation of ICON-MIGHTI thermospheric wind observations: 1. Nighttime Red-line Ground-Based Fabry-Perot Interferometers. *Journal of Geophysical Research*, *126*. https://doi.org/10.1029/2020JA028726

Richmond, A. D. (1973), Equatorial electrojet-1. Development of a model including winds and instabilities, J. Atmos. Terr. Phys., 35, 1083– 1103. https://doi.org/10.1016/0021-9169(73)90007-X

Richmond, A. D. (2021). Joule heating in the thermosphere. In W. Wang, & Y. Zhang (Eds.), Eds., Space physics and aeronomy collection volume 4. Upper atmosphere dynamics and energetics, Geophysical Monograph Series (Vol. 261). AGU. https://doi.org/10.1002/9781119815631.ch1

Richmond, A. D., and S. Matsushita (1975), Thermospheric Response to a Magnetic Substorm, J. Geophys. Res., 80, 2839-2850. https://doi.org/10.1029/JA080i019p02839

Sastri, J. H., R. Sridharan, and T. K. Pant (2003), Equatorial ionosphere thermosphere system during geomagnetic storms, in Disturbances in Geospace: The Storm-Substorm Relationship, Geophys. Monogr. Ser.,vol. 142, edited by A. S. Sharma, Y. Kamide, and G. S. Lakhina, pp. 185–203, AGU, Washington, D. C.. https://doi.org/10.1029/142GM16

Simi, K. G., S. V. Thampi, D. Chakrabarty, B. M. Pathan, S. R. Prabhakaran Nayar, and T. Kumar Pant (2012), Extreme changes in the equatorial electrojet under the influence of interplanetary electric field and the associated modification in the low-latitude F region plasma distribution, J. Geophys. Res.,117, A03331. https://doi.org/10.1029/2011JA017328

Somayajulu, V. V., C. A. Reddy, and K. S. Viswanathan (1987), Penetration of magnetospheric convective electric field to the equatorial ionosphere during the substorm of March 22, 1979, Geophys. Res. Lett., 14, 876-879. https://doi.org/10.1029/GL014i008p00876

Themens, D.R., Watson, C., Zagar, N., Vasylkevych, S., Elvidge, S., McCaffrey, A., Prikryl P., Reid, B., Wood A., & Jayachandran P.T. (2022). Global propagation of ionospheric disturbances associated with the 2022 Tonga volcanic eruption. *Geophysical Research Letters.*, https://doi.org/10.1029/2022GL098158

Wolf, R. A., R.W. Spiro, S. Sazykin, and F.R.Toffoletto (2007), How the Earth's inner magnetosphere works: An evolving picture, Journal of Atmospheric and Solar-Terrestrial Physics, 69, 288–302. https://doi.org/10.1016/j.jastp.2006.07.026

Yamazaki, Y., A. D. Richmond, A. Maute, H.-L. Liu, N. Pedatella, and F. Sassi (2014), On the day-to-day variation of the equatorial electro-jet during quiet periods, J. Geophys. Res. Space Physics,119, 6966–6980. http://doi.org/10.1002/2014JA020243

Yamazaki, Y., Harding, B. J., Stolle, C., & Matzka, J. (2021). Neutral wind profiles during periods of eastward and westward equatorial electrojet. Geophysical Research Letters, 48, e2021GL093567. https://doi.org/10.1029/2021GL093567

Yizengaw, E., & Groves, K. M. (2018), Longitudinal and seasonal variability of equatorial ionospheric irregularities and electrodynamics, Space Weather, 16, 946–968. https://doi.org/10.1029/2018SW001980

Yizengaw, E., M. B. Moldwin, E. Zesta, C. M. Biouele, B. Damtie, A. Mebrahtu, B. Rabiu, C. F. Valladares, and R. Stoneback (2014), The longitudinal variability of equatorial electrojet and vertical drift velocity in the African and American sector, Ann. Geophys., 32, 231–238. https://doi.org/10.5194/angeo-32-231-2014

Yizengaw, E., M. B. Moldwin, E. Zesta, M. Magoun, R. Pradipta, C. M. Biouele, A. B. Rabiu, O. K. Obrou, Z. Bamba, and E. R. de Paula (2016), Response of the equatorial ionosphere to the geomagnetic DP 2 current system, Geophys. Res. Lett., 43, 7364–7372. https://doi:10.1002/2016GL070090

Yuen, D.A., Scruggs, M.A., Spera, F.J., Zheng, Y., Hu, H., McNutt, S.R., Thompson, G., Mandli, K., Keller, B.R., Wei, S.S., Peng, Z., Zhou, Z., Mulargia, F., Tanioka, Y., Under the Surface: Pressure-Induced Planetary-Scale Waves, Volcanic Lightning, and Gaseous Clouds Caused by the Submarine Eruption of Hunga Tonga-Hunga Ha'apai Volcano Provide an Excellent Research Opportunity, Earthquake Research Advances. https://doi.org/10.1016/j.eqrea.2022.100134

Zhang, S.-R., Vierinen, J., Aa, E., Goncharenko, L.P., Erickson, P.J., Rideout, W., Coster, A.J., & Spicher, A. (2022). 2022 Tonga volcanic eruption induced global propagation of ionospheric disturbances via Lamb waves. *Frontiers in Astronomy and Space Sciences*, *9:*871275. https://doi.org/10.3389/fspas.2022.87125

Figure 1. The IMF/solar wind conditions and SYM-H index for 13-16 January 2022.

Figure 2. An overview of the observations on 13-17 January 2022. (a) Swarm A magnetic field perturbations. (b) Ground-based magnetic field perturbations. (c) Expanded view of the magnetic field perturbations from Swarm A and B on 15 January. (d) Geographic locations and universal times of the observations on 15 January.

Figure 3. MIGHTI daytime zonal winds along 7 ICON orbits on 15 January 2022. (a) Altitude profiles of zonal wind sequences. (b) Averaged zonal wind profiles. (c) The sequences of zonal wind observations at ~103 km altitude versus longitude from two days.

Figure 4. (a) Schematic illustration of the E- and F-region ionosphere responses to a large-scale disturbance propagating eastward from the Tonga eruption site. (b) Summary of the timelines of the observed features by the propagating disturbance.

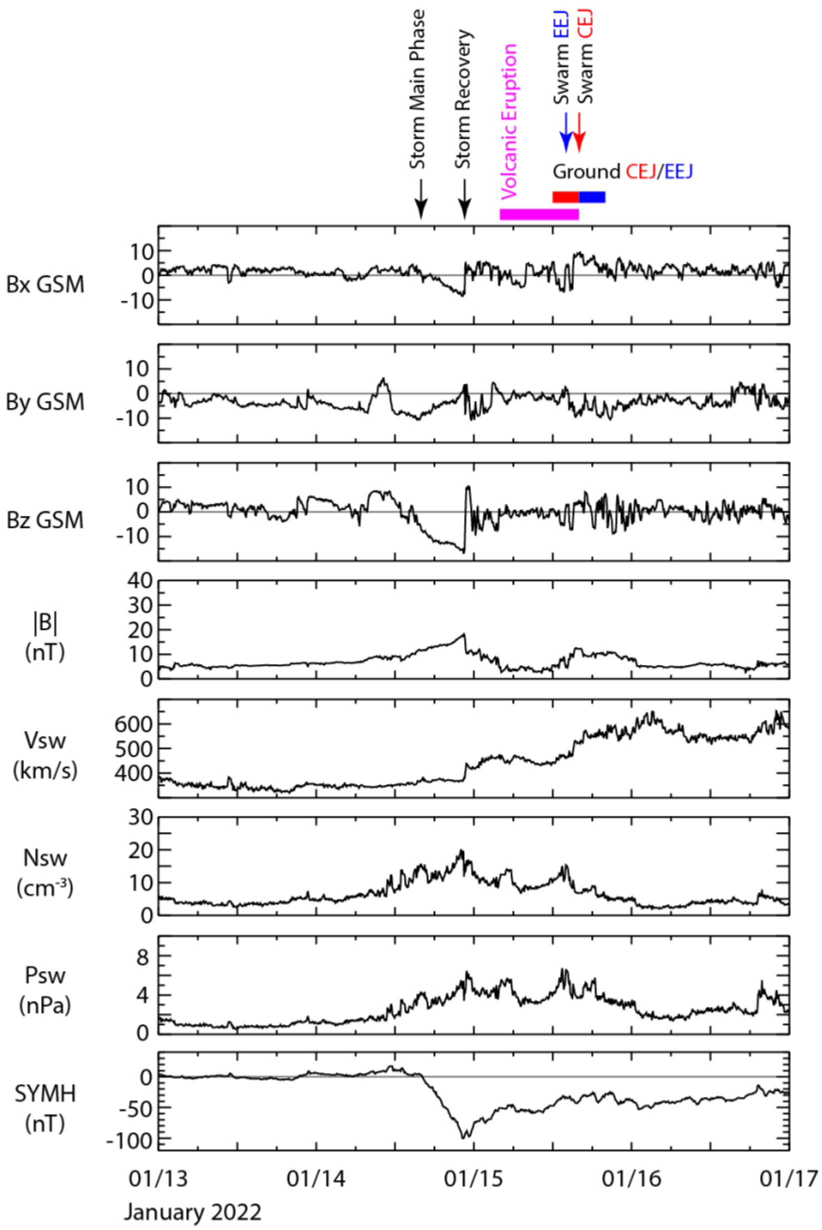

Figure 1

Figure 1. The IMF/solar wind conditions and SYM-H index for 13-16 January 2022.

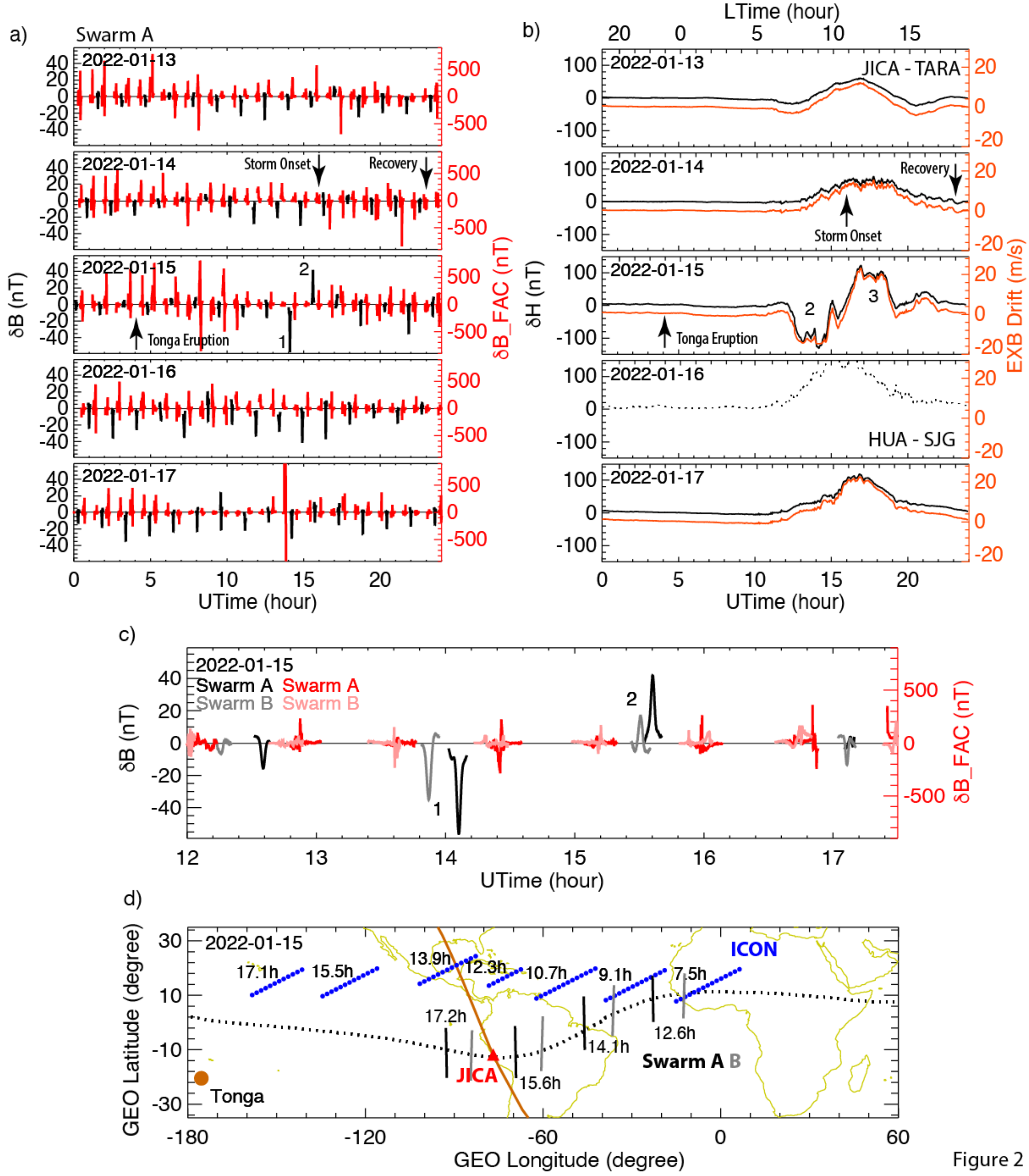

Figure 2. An overview of the observations on 13-17 January 2022. (a) Swarm A magnetic field perturbations. (b) Ground-based magnetic field perturbations. (c) Expanded view of the magnetic field perturbations from Swarm A and B on 15 January. (d) Geographic locations and universal times of the observations on 15 January.

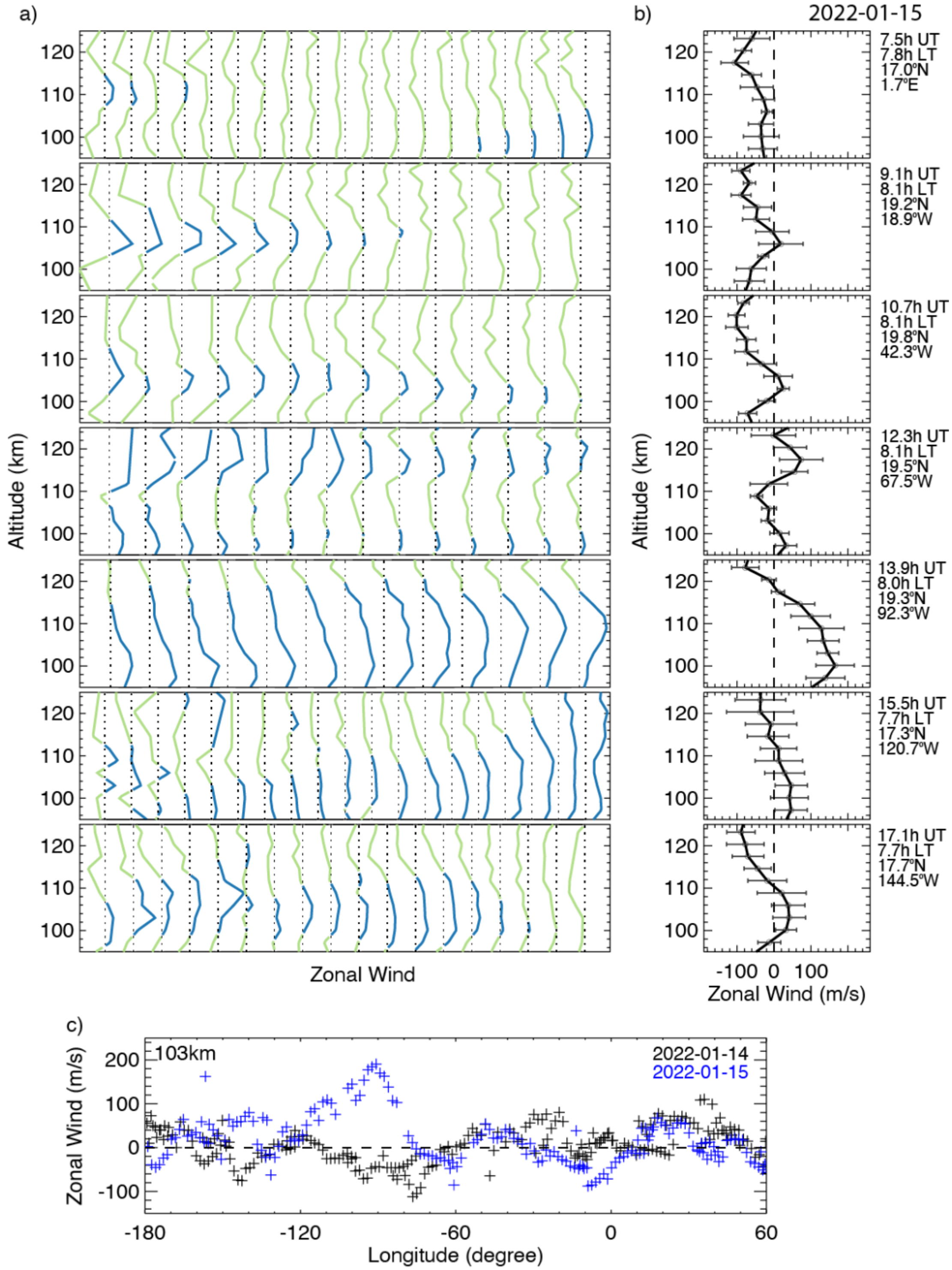

Figure 3. MIGHTI daytime zonal winds along 7 ICON orbits on 15 January 2022. (a) Altitude profiles of zonal wind sequences. (b) Averaged zonal wind profiles. (c) The sequences of zonal wind observations at ~103 km altitude versus longitude from two days.

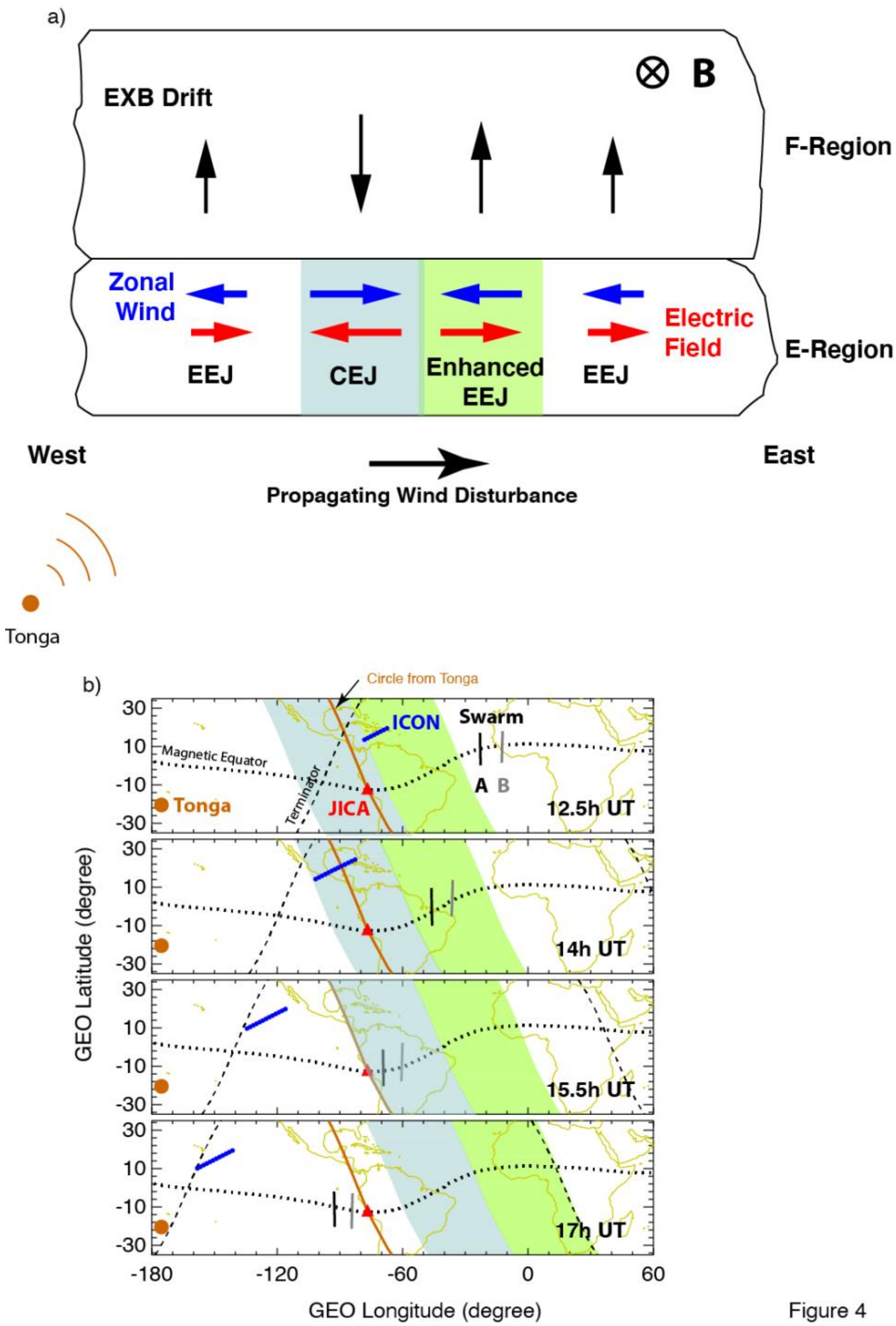

Figure 4

Figure 4. (a) Schematic illustration of the E- and F-region ionosphere responses to a large-scale disturbance propagating eastward from the Tonga eruption site. (b) Summary of the timelines of the observed features by the propagating disturbance.